Received 29 September 2021; revised 26 November 2021; accepted 5 January 2022.
Date of publication 12 January 2022; date of current version 14 February 2022.

Digital Object Identifier 10.1109/OJUFFC.2022.3142710

Air-Coupled Ultrasonic Spiral Phased Array for High-Precision Beamforming and Imaging

GIANNI ALLEVATO, (Student Member, IEEE), MATTHIAS RUTSCH, (Graduate Student Member, IEEE), JAN HINRICHS, (Graduate Student Member, IEEE), CHRISTOPH HAUGWITZ, (Student Member, IEEE), RAPHAEL MÜLLER, MARIUS PESAVENTO, (Senior Member, IEEE), AND MARIO KUPNIK, (Senior Member, IEEE)

Department of Electrical Engineering and Information Technology, Technische Universität Darmstadt, 64289 Darmstadt, Germany
CORRESPONDING AUTHOR: G. ALLEVATO (gianni.allevato@tu-darmstadt.de)

ABSTRACT Sparse spiral phased arrays are advantageous for many emerging air-coupled ultrasonic applications, since grating lobes are prevented without being constrained to the half-wavelength element spacing requirement of well-known dense arrays. As a result, the limitation on the maximum transducer diameter is omitted and the aperture can be enlarged for improving the beamforming precision without requiring the number of transducers to be increased. We demonstrate that in-air imaging, in particular, benefits from these features, enabling large-volume, unambiguous and high-resolution image formation. Therefore, we created an air-coupled ultrasonic phased array based on the Fermat spiral, capable of transmit, receive and pulse-echo operation, as well as 3D imaging. The array consists of 64 piezoelectric 40-kHz transducers (Murata MA40S4S), spanning an aperture of 200 mm. First, we provide an application-independent numerical and experimental characterization of the conventional beamforming performance of all operation modes for varying focal directions and distances. Second, we examine the resulting imaging capabilities using the single line transmission technique. Apart from the high maximum sound pressure level of 152 dB, we validate that unambiguous high-accuracy 3D imaging is possible in a wide field of view ($\pm 80°$), long range (20 cm to 5 m+) and with a high angular resolution of up to 2.3°. Additionally, we demonstrate that object shapes and patterns of multiple reflectors are recognizable in the images generated using a simple threshold for separation. In total, the imaging capabilities achieved are promising to open up further possibilities, e.g. robust object classification in harsh environments based on ultrasonic images.

INDEX TERMS Air-coupled, ultrasound, sparse array, spiral array, phased array, imaging, sonar.

I. INTRODUCTION

AIR-COUPLED ultrasound is applied in a wide variety of areas such as agriculture [1], [2], food analysis [3], [4], power transfer [5]–[7], communications [8], [9], range finding [10]–[12] and non-destructive testing [13]–[15]. Here, ultrasonic phased arrays become increasingly popular due to their high achievable sound intensity and their ability to steer and focus the sound beam. By utilizing ultrasonic arrays, further applications have emerged such as tactile displays [16]–[18], particle levitation [19]–[21], parametric loudspeakers [22]–[24] and in-air imaging [25]–[29].

In these applications, dense regular-grid array geometries are most commonly used. Therefore, the inter-element spacing is required to be at maximum half wavelength ($\lambda/2$). Otherwise, grating lobes are formed, leading to ambiguous beamforming, resulting in high-intensity sound emission in undesired directions. Consequently, two design limitations arise from the $\lambda/2$ criterion of dense arrays. First, the achievable array aperture size is constrained by the number of transducers used. Second, the diameter of the transducer type must not be wider than $\lambda/2$.

However, many of the air-coupled array applications mentioned use too large piezoelectric transducers (e.g. Murata MA40S4S, Prowave 400ST), since they have excellent characteristics for operation in air. They provide a high sound pressure level with a low operating frequency of 40 kHz,

resulting in lower attenuation by the medium [30]. Additionally, they are easy to drive, thus reducing the complexity and cost of the overall array electronics. Still, the benefits come at the expense of grating lobe formation.

We addressed this problem in previous work by creating a 3D-printed waveguide containing 64 acoustic ducts into which the piezoelectric transducers are inserted [31]–[36]. In this way, the effective inter-element spacing is reduced to $\lambda/2$, enabling grating lobe free beamforming while providing additional protection in harsh environments [37]. However, as the effective array aperture is reduced as well, the -3 dB main lobe width (MLW) is widened, thus lowering the beamforming precision.

In order to overcome both design limitations of dense arrays on the allowed transducer diameter and achievable array aperture size, sparse array geometries are a viable option. Due to their irregular aperiodic element positioning, the formation of grating lobes is prevented even at greater inter-element spacings. As a result, the array aperture can be enlarged for improving the beamforming precision without requiring the number of transducers to be increased [38]–[40].

In particular, sparse spiral arrays based on the Fermat spiral feature advantageous properties [41]–[43]. First, the simple deterministic design allows a flexible customization to the requirements of the application. Second, the MLW and maximum side lobe level (MSLL) can additionally be fine-tuned by density tapering [42]. Third, the suppression of grating lobes is independent of the frequency used, thus unambiguous beamforming is ensured for narrow- and broadband signals [43].

Spiral phased arrays have been increasingly investigated in various domains ranging from satellite communication [42], radar [44], microwave imaging [45] and optical phased arrays [46], over noise source localization [47], [48] to medical ultrasound [49]–[52]. For air-coupled ultrasonic applications, they have been examined for the transmit-only generation of haptic feedback [53], for NDT using receive-only microphone arrays [54] and for the detection of pasture biomass and grape clusters using two dedicated transmit and receive arrays without beam steering [55], [56].

In this article, we demonstrate that ultrasonic in-air imaging, in particular, benefits from the advantages of spiral geometries allowing unambiguous high-resolution image formation. Therefore, we created an air-coupled fully-steerable spiral phased array supporting transmit (TX), receive (RX) and pulse-echo (PE) operation, as well as 3D imaging. The array consists of 64 Murata MA40S4S transducers, whose inter-element spacings are all greater than $\lambda/2$, thus spanning an enlarged aperture of 200 mm for demonstrating the grating lobe suppression and high beamforming precision. We investigate its real-world beamforming behavior and the resulting in-air imaging capabilities by providing an in-depth experimental and simulated characterization. The main contributions are grouped into two categories. First, an application-independent characterization of the TX, RX, and PE performance is conducted to analyze the beamforming precision and accuracy, and to identify the main differences between measurements and simulations. These results further provide a starting point for future works investigating other applications. Second, the general findings are put into application context by examining the resulting in-air imaging capabilities with a high angular resolution of up to 2.3°, extending our preliminary work [57].

The article is structured as follows: Section II outlines the phased array system architecture and describes the control and processing of the three operation modes plus the image formation. In addition, the simulation model for referencing the experiments is explained. In Section III, we elaborate the abovementioned experimental characterization and discuss the results. We draw the conclusions and provide an outlook for future work in Section IV.

II. METHODS

In this section, we introduce the four main components of the phased array system and describe the processing of the different operation modes, i.e. TX, RX and PE, as well as the image generation. In addition, the simulation model, used as a reference for the subsequent experiments in Section III, is presented.

A. ARRAY AND SYSTEM DESIGN

The system consists of the ultrasonic phased array, custom transceiver electronics, an FPGA system-on-chip board (Avnet MicroZed) and an external PC.

The phased array is composed of $M = 64$ piezoelectric air-coupled ultrasonic transducers (Murata MA40S4S, $\phi 10$ mm) with a resonant frequency of 40 kHz and a narrow bandwidth of 1.2 kHz. The transducers are arranged on the xy-plane on a single PCB along the Fermat spiral spanning an overall aperture with a diameter of $D_{\text{ap}} = 200$ mm (Fig. 1). The position of the m-th transducer $\mathbf{r}_m$ is defined by sampling the Fermat spiral, that is

$$(R_m, \phi_m) = \left(R_{\text{ap}} \sqrt{\frac{m}{M-1}},\ 2\pi m \frac{1+\sqrt{V}}{2} \right), \text{ and} \quad (1)$$

$$\mathbf{r}_m = R_m \left[\cos(\phi_m), \sin(\phi_m), 0 \right], \quad (2)$$

where $M = 64$ is the number of transducers, $m \in [0, \ldots, M-1]$ is the transducer index, R_m is the radius to the aperture center and ϕ_m is the corresponding angle, $R_{\text{ap}} = D_{\text{ap}}/2$ is the maximum aperture radius and $V = 5$ is a design parameter that determines the angular distance between two successive elements and therefore the number and position of the spiral arms. By choosing $V = 5$, the angular distances correspond to the Golden Angle, resulting in the so-called sunflower pattern. This pattern features a uniform spatial density of the transducer positions where all angles ϕ_m are unique due to the Golden Angle being an irrational number [42], [50]. In [43], spiral array configurations with different V values are analyzed with

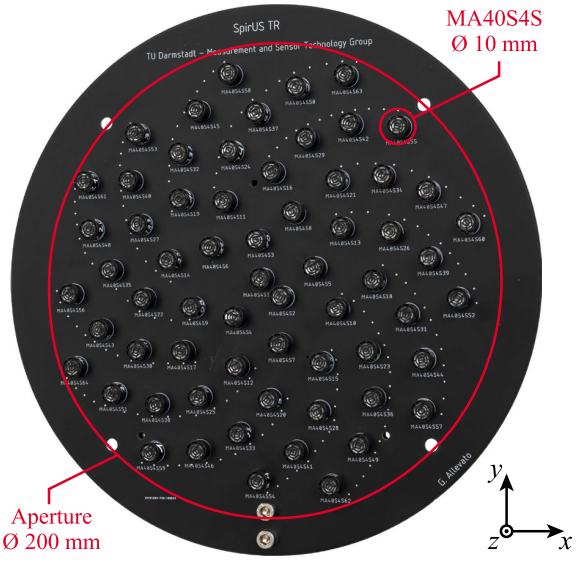

FIGURE 1. The spiral phased array consists of 64 ultrasonic 40-kHz narrow-band transducers. Each transducer can be used for transmit, receive and pulse-echo operation. Although the inter-element spacings are greater than λ/2, the spiral geometry prevents the formation of grating lobes. The enlarged aperture enables high-precision beamforming.

the conclusion that $V = 5$ gives Pareto optimal results in terms of MLW and MSLL. Density and amplitude tapering, as proposed in [42], [43], [50], are not applied to maintain a balanced ratio between MLW and MSLL and to avoid limiting the radiation power and sensitivity. With the selected diameter of $D_{\mathrm{ap}} = 200\,\mathrm{mm}$ (23.3 λ), the expected MLW is halved from 5.2° to 2.6°, compared to the smallest possible aperture diameter $D_{\mathrm{ap,\,min}} = 100\,\mathrm{mm}$ (11.7 λ), limited by the size of the transducers. However, a further halving of the MLW requires a further doubling of the aperture diameter. Therefore, a reasonable trade-off between the achievable MLW and simple manufacturing as well as integrability into our existing measurement setup is found.

The remaining system components, i.e. transceiver electronics, the FPGA board and the PC, are described in detail in [36] and are summarized with the key aspects hereafter. The transceiver electronics provides a dedicated transmit and receive channel for each of the 64 transducers, allowing individual time-delayed excitation with unipolar square-wave burst signals (1 ms, 20 V_{pp}, 40 kHz) and individual sampling of the transducer signals (195 kSa/s, 12 bit). The FPGA SoC (Xilinx Zynq 7010) is used for sequence control, signal generation and acquisition, and ethernet communication with the PC, where the signals are processed and analyzed using *Matlab*. All together, the system described supports fully steerable TX and RX beamforming, and therefore in combination, also acoustic imaging using PE detection.

B. OPERATION MODES AND IMAGE FORMATION

Next, we explain the specific control and processing of the three operation modes TX, RX and PE. For this, apart from unfocused beams for far-field beamforming, focused beams are considered as well, due to the large aperture and the resulting near-field, ranging from 0 m to approximately 1.16 m. In the right-handed coordinate system used, the origin is at the array center, all array elements are in the xy-plane, the transducer apertures are facing in the positive z direction, and the xz-plane is horizontal (Fig. 1). A point $\mathbf{r}$ in the coordinate system is described by

$$\mathbf{r} = R\left[\sin(\theta)\cos(\varphi),\, \sin(\varphi),\, \cos(\theta)\cos(\varphi)\right], \tag{3}$$

where R is the Euclidean distance from the array center, θ is the azimuth, and φ is the elevation angle.

Focused TX beamforming to a specific point r_{foc} in the region of interest (ROI) is performed by driving all transducers with individually time-delayed square-wave signals, where the time delay of the m-th transducers signal $s_{\mathrm{TX},m}(t) = s_{\mathrm{TX}}\,(t - \Delta t_{\mathrm{foc},m})$ is calculated with

$$\Delta t_{\mathrm{foc},m}(r_{\mathrm{foc}}) = (R_{\mathrm{foc}} - R_{\mathrm{foc},m})/\mathrm{c}, \tag{4}$$

where $R_{\mathrm{foc}} = \|r_{\mathrm{foc}}\|_2$ is the focal distance from the array center, c is the speed of sound and $R_{\mathrm{foc},m} = \|\, r_{\mathrm{foc}} - r_{\mathrm{m}}\,\|_2$ is the distance from the m-th transducer center to the focal point [58].

For unfocused TX beamforming, the beam is not directed to a specific point, but in a specific direction $(\theta_{\overline{\mathrm{foc}}}, \varphi_{\overline{\mathrm{foc}}})$. The focal distance consequently lies at infinity. The calculation of the time delay of the m-th transducer $\Delta t_{\overline{\mathrm{foc}},m}$ is given without focal distance R_{foc}, that is

$$\Delta t_{\overline{\mathrm{foc}},m} = \left[x_m \sin(\theta_{\overline{\mathrm{foc}}})\cos(\varphi_{\overline{\mathrm{foc}}}) + y_m \sin(\varphi_{\overline{\mathrm{foc}}})\right]/\mathrm{c}, \tag{5}$$

where (x_m, y_m) are the coordinates of the m-th transducer corresponding to (2). For both methods, focused and unfocused TX beamforming, the respective minimum values are subtracted from the time delays of all transducers, so that all values are positive, thus causal.

In RX mode, first the $(M \times N)$ raw signal matrix S_{RX} is obtained, where M is the number of transducers and N is the number of samples acquired. The frequency spectrum $\hat{\mathbf{S}}_{\mathrm{RX}}$ of each transducer signal is formed and multiplied element-wise with the frequency response of the matched filter $\hat{\mathbf{h}}$ corresponding to the transmitted pulse for pre-processing, that is

$$\hat{\mathbf{S}}_{\mathrm{RX},\,(m,:)} = \mathscr{F}_N\left\{\mathbf{S}_{\mathrm{RX},\,(m,:)}\right\} \odot \hat{\mathbf{h}}, \tag{6}$$

for $m = 0, \ldots, M-1$. Using narrow-band conventional beamforming, we obtain the spatially filtered spectrum for a given focal point, that is

$$\hat{\mathbf{s}}_{\mathrm{foc}}(\mathbf{r}_{\mathrm{foc}}) = \mathbf{w}^{\mathsf{H}}_{\mathrm{foc}}(\mathbf{r}_{\mathrm{foc}})\,\hat{\mathbf{S}}_{\mathrm{RX}}, \tag{7}$$

where $\mathbf{w}^{\mathsf{H}}_{\mathrm{foc}}$ is the $(1 \times M)$ beamforming vector [59] whose m-th element is given by

$$\mathbf{w}^{\mathsf{H}}_{\mathrm{foc},m}(\mathbf{r}_{\mathrm{foc}}) = \exp\left[-\mathrm{j}2\pi f_0 \Delta t_{\mathrm{foc},m}(\mathbf{r}_{\mathrm{foc}})\right], \tag{8}$$

where $f_0 = 40\,\mathrm{kHz}$ is the resonance frequency of the transducers. In order to obtain the unfocused beamforming vector, in (8) $\Delta t_{\mathrm{foc},m}$ is replaced with $\Delta t_{\overline{\mathrm{foc}},m}$. Subsequently, the

spatially filtered analytic spectrum is transformed back into the time domain using IFFT and its envelope is generated by forming the absolute value of each element, that is

$$\mathbf{s}_{\mathrm{foc}}(\mathbf{r}_{\mathrm{foc}}) = \left| \mathscr{F}_N^{-1} \left\{ \hat{\mathbf{s}}_{\mathrm{foc}}(\mathbf{r}_{\mathrm{foc}}) \right\} \right|. \tag{9}$$

In PE mode, the TX and RX beamforming modes are combined. For this purpose, a focused or unfocused 40-kHz pulse with a length of $T_{\mathrm{pulse}} = 1$ ms is transmitted to the focal point or direction by driving all transducers with time-delayed signals according to (4) and (5), respectively. After the pulse transmission, the T/R switches activate the RX mode, the received signals S_{RX} are acquired by all transducers, pre-processed and spatially filtered by focused or unfocused RX beamforming, as in (7), to the same focal point or direction, respectively.

For imaging, we use the PE mode described and sequentially scan the discretized ROI line-by-line, i.e. single line transmission (SLT). The ROI is defined with a field of view, i.e. a set of K focal points or directions, and a range of view R_{v}, which determines the number of acquired samples $N = \lfloor 2\,(R_{\mathrm{v}}/\mathrm{c})\,f_{\mathrm{s}} \rfloor$. For each focal point or direction, a pulse-echo event is performed. The spatially filtered envelopes obtained are then color coded, rendered at their corresponding origin position and linearly interpolated to produce 2D or 3D scans. More information about the generation of the acoustic images is provided in [33].

The SLT imaging method is applicable in the near-field and far-field and is suitable for long-range imaging due to the array gains during transmission and reception. In addition, the two-fold spatial filtering lowers the MSLL, thus, improves the suppression of side lobe artifacts. Other imaging methods, e.g. synthetic aperture focusing [60], diverging waves [61], multi line acquisition [62], used to improve the frame rate, are part of future work and are not considered in this article.

C. SIMULATION MODEL

In order to evaluate the results of the subsequent experiments (Section III) and to identify differences from the expectations, we provide a model for the real measurements. The model is based on the discretized and normalized well-known Rayleigh integral, which computes the superimposed magnitude $p(r_{\mathrm{P}}, r_{\mathrm{foc}})$ for a specific spatial position of a point receiver or source r_{P} in dependence of a particular beamforming focal point r_{foc}. Apart from the array geometry itself, the effective aperture of each transducer ($D_{\mathrm{ap},m} = 7$ mm) is considered as well by generating a mesh using *DistMesh* [63], which consists of $L = 362$ mesh points on a circular disk with an average spacing of $0.05\,\lambda$. In this way, the directivity of the single transducers is included. The model equations are given by

$$p(r_{\mathrm{P}}, r_{\mathrm{foc}}) = \left| \frac{1}{M} \sum_{m=0}^{M-1} p_m(r_{\mathrm{P}}) \mathbf{w}_{\mathrm{foc},m}^{\mathsf{H}}(\mathbf{r}_{\mathrm{foc}}) \right|, \text{ and} \tag{10}$$

$$p_m(r_{\mathrm{P}}) = \frac{1}{L} \sum_{l=0}^{L-1} \frac{1}{R_{\mathrm{P},(m,l)}} \exp\left[-\mathrm{j}2\pi \frac{f_0}{\mathrm{c}} R_{\mathrm{P},(m,l)} \right], \tag{11}$$

where $p_m(r_{\mathrm{P}})$ is the discretized integral over the mesh points of the m-th transducer aperture, $R_{\mathrm{P},(m,l)} = \| \mathbf{r}_{\mathrm{P}} - \mathbf{r}_{(m,l)} \|_2$ is the distance from the point receiver or source $\mathbf{r}_{\mathrm{P}}$ to the l-th mesh point position of the m-th transducer $\mathbf{r}_{(m,l)}$ and $\mathbf{w}_{\mathrm{foc},m}^{\mathsf{H}}$ is the beamforming factor of the m-th transducer (8). Therefore, with this model, the results obtained from the real measurement setups with a specific microphone or transmitter position $\mathbf{r}_{\mathrm{P}}$ and selected focal point $\mathbf{r}_{\mathrm{foc}}$ can be relatively referenced.

III. EXPERIMENTAL RESULTS AND DISCUSSION

The experiments are grouped into two categories. First, general application-independent characterizations of the TX, RX, and PE operation modes are conducted and compared to the simulation model. For each mode, we examine the 2D directivity patterns, the sectional directivity patterns for varying focal points in the near- and far-field, and the radial on-axis patterns for varying focal distances. From these patterns, we extract and discuss the most significant parameters, i.e. the magnitude at the focal point, the position of the focal peak, the MWL or focal length, and the angular or radial MSLL. Second, we address the more specific use case of acoustic imaging. Here, we validate the angular resolution and evaluate the imaging of multi-reflector scenarios in both, the far- and near-field.

A. MEASUREMENT SETUPS

All measurements are performed in an anechoic chamber. The spiral array including a rigid baffle is mounted on two rotational axes (Fig. 2). The rigid baffle is aligned with the output surfaces of the transducers. Therefore, the setup resembles the simulation model more accurately, for which an infinite rigid baffle is assumed. In front of the array, there is a linear axis (length of 6 m) with a movable slide onto which different targets can be mounted. Using the linear axis and the two rotational axes, the target can be freely positioned in the coordinate system of the array. The selection of the specific target depends on the array operation mode being examined. In TX mode the calibrated microphone (B&K Type 4138 and B&K Type 2670 preamplifier), in RX mode a pre-characterized ultrasonic transducer (Murata MA40S4S) and in PE mode either the corner reflector or one of the sphere reflectors is used as target (Fig. 2). Overall, the setup allows the automated and independent positioning of the target and focal point.

B. 2D DIRECTIVITY PATTERNS

The 2D directivity patterns show the direction-dependent magnitude distribution of the main and side lobes when beamforming, i.e. the main characteristics of the spatial filtering. We measure the far-field patterns of all three modes (TX, RX, PE) and compare them to the simulated pattern (Sim), (Fig. 3).

In TX mode, we use the calibrated microphone [Fig. 2(a)] as target positioned at a fixed distance of 5 m. The array sequentially transmits unfocused pulses (40 kHz, 1 ms)

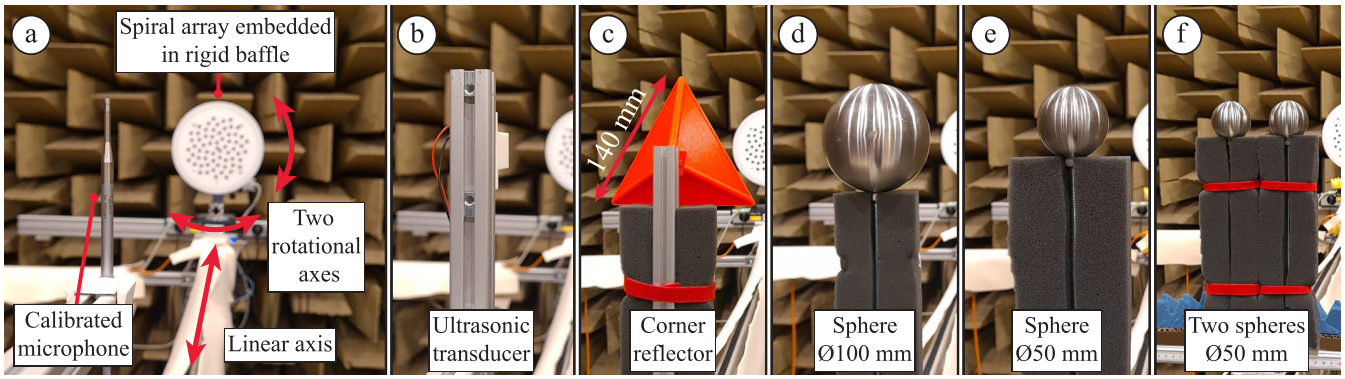

FIGURE 2. The measurement setup in the anechoic chamber allows the different targets to be positioned three-dimensionally in the coordinate system of the array. The positioning of the target and the focal point is fully-automated and independently controllable. The respective targets used are for TX mode measurements the calibrated microphone (B&K Type 4138) (a), for RX mode the pre-characterized ultrasonic transducer (Murata MA40S4S) (b) and for PE mode the corner reflector (c) or one of the sphere reflectors (d),(e). The double sphere setup on the transverse profile is used to measure the angular resolution (f).

steered to the fixed direction (0°, 0°). After each pulse transmission, the array is mechanically rotated in steps of 1° using the two rotational axes. The microphone aperture is not rotated, but always points to the array center. This way, the microphone is positioned at different directions of the array coordinate system until pulses from all angles of [Fig. 3(b)] are obtained. The corresponding maximum magnitude of the pulses received are plotted and linearly interpolated in the directivity pattern.

In RX mode, the same procedure is used, however the microphone is replaced with the pre-characterized ultrasonic transducer [Fig. 2(b)], sequentially transmitting pulses (40 kHz, 1 ms) to the array. The array signals are spatially filtered for direction (0°, 0°) using unfocused receive beamforming, while the array is mechanically rotated.

For measuring the PE directivity pattern, the corner reflector [Fig. 2(c)] is used as target and the unfocused TX and RX modes described are combined, i.e. two-fold spatial filtering is applied. The corner reflector has been selected as target as it creates a stronger echo compared to the spheres. Therefore, despite the doubled length of the propagation path (10 m), the echo of the reflector stands out from interfering echoes of the environment, caused by the sound absorbers at the walls, rail and mountings for example.

In all measured and simulated patterns (Fig. 3), there is a single narrow main lobe at the expected center direction (0°, 0°) and grating lobes do not form. The MLWs of the single patterns differ only slightly (3° for Sim, TX, RX and 2.5° for PE). There is a side-lobe-reduced zone surrounding the main lobe followed by a concentric ring of side lobes at approximately $\sqrt{\theta^2+\varphi^2} = 30°$. This ring contains the highest side lobes for all patterns, thus defining the respective MSLL, which also differs only slightly from the expected value, i.e. in dB for Sim −15, for TX −17, for RX −15.9, and for PE −26.7. The side lobe level of the PE pattern is overall lower and the MLW is slightly narrower, due to the two-fold spatial filtering. At the periphery of the patterns, where $\sqrt{\theta^2+\varphi^2} > 70°$, there is a major drop in side lobe level caused by the directivity of the individual transducers themselves. Since the color scale of the PE pattern is adjusted, the noise floor and scattering reflections of the room become visible in this zone.

In summary, primarily the exact positions and levels of the side lobes are different from the expected simulated patterns. The differences are caused by interfering room reflections, as well as relative amplitude and phase deviations between the individual transducers, which will be examined in future work. Nevertheless, all directivity patterns measured agree well with the prediction of the model and confirm the grating lobe free beamforming capability with high precision.

C. SECTIONAL DIRECTIVITY PATTERNS FOR VARYING FOCAL ANGLES

Next, the sectional directivity patterns with varying focal angles are measured to analyze the influence on the magnitude at the focal angle, the angle of the focal peak, the MLW and MSLL. The parameters examined indicate the direction-dependent precision and accuracy of the beamforming. All three modes (TX, RX and PE) are considered in the far-field (5 m) and in the near-field (0.2 m), and are compared to the simulation (Sim). A similar measurement procedure as in Section III-B is used with the following differences. First, for each mechanical rotation the focal angle is varied sequentially between 0° and 90° in steps of 5°. Second, the focal distance is either at infinity (unfocused) for the far-field measurement or focused at the target distance (0.2 m) for the near-field measurement. Third, the step size of the mechanical rotation is reduced to 0.5°, but limited to the horizontal plane (azimuth) due to the high amount of data generated and increased measurement duration. All measurements are repeated five times to identify possible deviations of the parameters examined. The targets used for the respective modes are the microphone (TX) [Fig. 2(a)], the transducer (RX) [Fig. 2(b)], the corner reflector (far-field PE) [Fig. 2(c)]

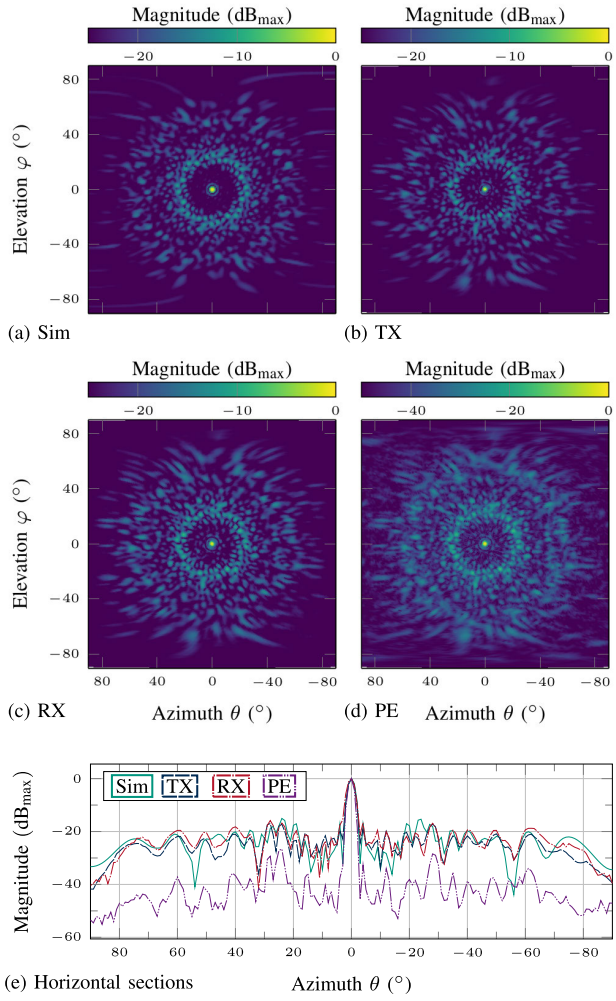

FIGURE 3. The 2D directivity patterns are measured in the far-field (5 m) and show the magnitude distribution of the main and side lobes for a steering angle of (0°,0°), i.e. the main characteristics of the spatial filtering. The targets used are the microphone for TX, the ultrasonic transducer for RX and the corner reflector for PE [Fig. 2(a),(b),(c)]. All directivity patterns measured (b)-(d) agree well with the prediction of the simulation (a) and confirm the grating lobe free high-precision beamforming capability. For easy comparison, the color scale of the PE pattern is adjusted by 0.5 due to two-fold spatial filtering.

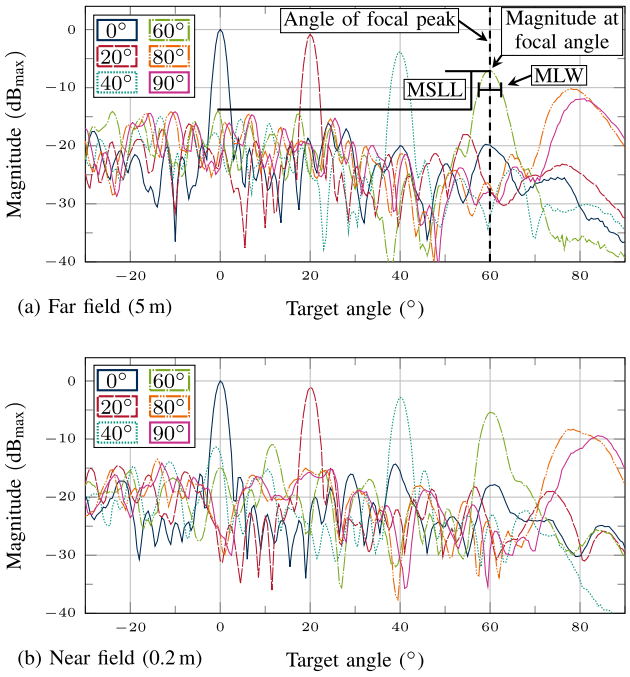

FIGURE 4. Sectional directivity patterns of the TX mode, as an example (non-averaged), for varying focal angles in the near- and far-field. The MLW widens, the MSLL rises, and the magnitude of the focal peak lowers for increasing focal angles. The angle of the focal peak deviates from desired high focal angles (80°, 90°). Thus, the beamforming precision and accuracy in the periphery is reduced. The parameters labeled are compared in (Fig. 5) for all operation modes.

and the small sphere (near-field PE) [Fig. 2(e)]. In the near-field measurement, the small sphere is advantageous due to its smaller retroreflective area, so that the measurement of the MLW is less influenced by the reflector dimension.

The sectional directivity patterns of the TX mode measured in the far- and near-field are shown as an example for selected focal angles in (Fig. 4). For both measurements, the -3 dB main lobe width widens with increasing focal angle, thus decreasing the precision and selectivity of the beamforming. In addition, the magnitude at the focal angle decreases, mainly due to the directivity of the individual transducers. As a result, the MSLL degrades as well, since peripheral main lobes are more attenuated by the directivity than centrally located side lobes. All these effects additionally cause a mismatch between the angle of the focal peak and the desired focal angle, so that the accuracy of the beamforming decreases with increasing focal angle.

For easy comparison, instead of presenting the directivity patterns of all operation modes and focal angles, we only extract the key parameters, i.e. the magnitude at the focal angle, the angle of the focal peak, MLW and MSLL, as a function of focal angle for the near- and far-field (Fig. 5).

The magnitudes at the focal angle decrease for all operation modes, in the near-field and far-field with increasing focal angle [Fig. 5(a1),(b1)]. The decrease measured mostly agrees well with the prediction of the simulation, as it includes the aperture of the single transducers. However, there are differences to the simulation, primarily for peripheral focal angles $|\theta| > 80°$, where the magnitudes measured drop more severely. The cause is the housing of the transducer elements, which is not taken into account by the simulation model. The PE magnitudes at the focal angle show a significantly steeper drop, since the pulse is affected twice by the directivity of the single transducers, when transmitting and when receiving. Overall, the transducer directivity causes a slightly higher attenuation of the magnitudes at the focal angle in the far-field than in the near-field.

The angle of the focal peak agrees well with the desired focal angle for all measurements and the simulation up to $|\theta| < 75°$, confirming a high beamforming accuracy [Fig. 5(a2),(b2)]. For focal angles higher than 75°, the angle of the focal peak is lower than the desired focal angle and is limited to approximately 80° and 83° for the far-field and near-field measurements, respectively. This limitation is again caused by the directivity of the single transducers, which strongly attenuates the magnitude for high focal angles. Therefore, the simulated angle of the focal peak reaches a higher limit (86°), since the increased attenuation by the transducer housing is not included. In summary, these results imply that the beamforming capability for TX, RX and PE is accurate but constrained to the respective limits for the near- and far-field.

The MLW widens with increasing focal angle, thus reducing the beamforming precision [Fig. 5(a3),(b3)]. All measurements are close to the expected values from the simulation. The MLW is between 2° and 5° up to a focal angle of $|\theta| < 55°$ followed by a more pronounced widening with increasing focal angle. The PE MLW is slightly narrower for all focal angles due to the two-fold spatial filtering. The difference for the TX and RX modes to the simulated MLW is within $\pm 1°$ up to a focal angle of $|\theta| < 80°$. In the far-field, the MLWs of all modes and the simulation reach a plateau at approximately $|\theta| = 80°$ above which the MLW widens only slightly. The plateau is mainly caused by the directivity from [Fig. 5(b1)], which attenuates the main lobe for high focal angles preventing further widening. A similar characteristic is observed in the near-field, but the plateau is followed by a narrowing. The narrowing is primarily due to the notch in the directivity at 80° [Fig. 5(a1)], where the main lobe is selectively attenuated, thus affecting the −3 dB width. However, the overall differences in MLW between the near- and far-field measurements are only minor.

The MSLL degrades with increasing focal angle, as a result of the directivity of the single transducers [Fig. 5(a4),(b4)]. The TX and RX MSLL measurements in the near- and far-field show only a slight deviation from the simulation of approximately ±2 dB. The PE MSLL is in general approximately two times lower in dB scale than the TX and RX MSLL due to the two-fold spatial filtering, as expected. In order to obtain accurate MSLL results, the suppression of interfering reflections by covering mountings with foam absorbers is mandatory. Otherwise, false sidelobes can be created impairing the measurement. For all extracted parameters, the standard deviations obtained from five measurements do not show significant irregularities.

In the context of acoustic imaging with the PE method, the parameters measured have the following effects. The MLW significantly determines the angular resolution, indicating the minimum angular distance between two reflectors required, such that they can be imaged separately. Therefore, two peripherally positioned reflectors are required to have a greater angular distance from each other for separability, compared to two centrally positioned reflectors. Since the angular resolution is approximately constant with distance, objects can be imaged with improved absolute resolution if they are close to the array, as demonstrated in Section III-F.

The deviations between the selected focal angle and the resulting angle of the focal peak cause peripherally located reflectors to be imaged at an incorrect angle. For example, reflectors located at ±80° will additionally be rendered to an angle of ±90° in the image.

Furthermore, the decrease of the magnitude at the focal angle causes two identical reflectors to be imaged with different magnitudes despite the same reflectivity, if one is placed centrally and one peripherally. In conjunction with the increasing MSLL, the detected echo of the peripheral reflector stands out less prominently from the side lobe artifacts caused by the centrally located reflector. Therefore, the dynamic range in the peripheral region is reduced: If a reflector is located in the center of the ROI, weaker peripheral reflectors are particularly difficult to detect. In addition, when many reflectors are present in the ROI, their side lobe artifacts will superimpose, thus reducing the dynamic range in the entire image, which can result in false detections. This effect is investigated in Section III-F with multi-reflector setups.

D. RADIAL ON-AXIS PATTERN FOR VARYING FOCAL DISTANCES

Similar to the sectional directivity patterns for different focal angles, we examine the radial on-axis patterns for different focal distances. All three operation modes (TX, RX, PE) are considered and compared with the simulation model (Sim). Instead of mechanically rotating the array, only the distance to the target is increased sequentially in steps of 1 cm from 3 cm up to 3 m using the linear axis. For each target distance, the beamforming focal distance is varied from 10 cm to 3 m in steps of 10 cm. In addition, the focal distance at infinity (unfocused beamforming) is considered. The targets of the respective modes are the microphone [Fig. 2(a)], receiving pulses from the array (TX), the ultrasonic transducer [Fig. 2(b)], transmitting pulses to the array (RX) and the sphere (ϕ100 mm) [Fig. 2(d)], reflecting the pulses back to the array (PE). The larger sphere (ϕ100 mm) has been chosen for the PE measurement as it provides a higher echo amplitude than the small sphere (ϕ50 mm) and is therefore suitable in the near- and far-field, since it stands out more from interfering room reflections. Moreover, unlike the corner reflector, the sphere has a well-defined reflection point.

The maximum magnitudes of the received pulses are evaluated, which all have a duration of 1 ms, a frequency of 40 kHz and are excited using 20 V_{pp}. All measurements are repeated five times to identify possible deviations of the parameters examined. From the radial on-axis patterns obtained, we analyze the four key parameters, i.e. magnitude at the focal distance, the distance of the focal peak, the focal length, and the MSLL out of the focal point. These parameters provide information on the distance-dependent precision and accuracy of the focused beamforming.

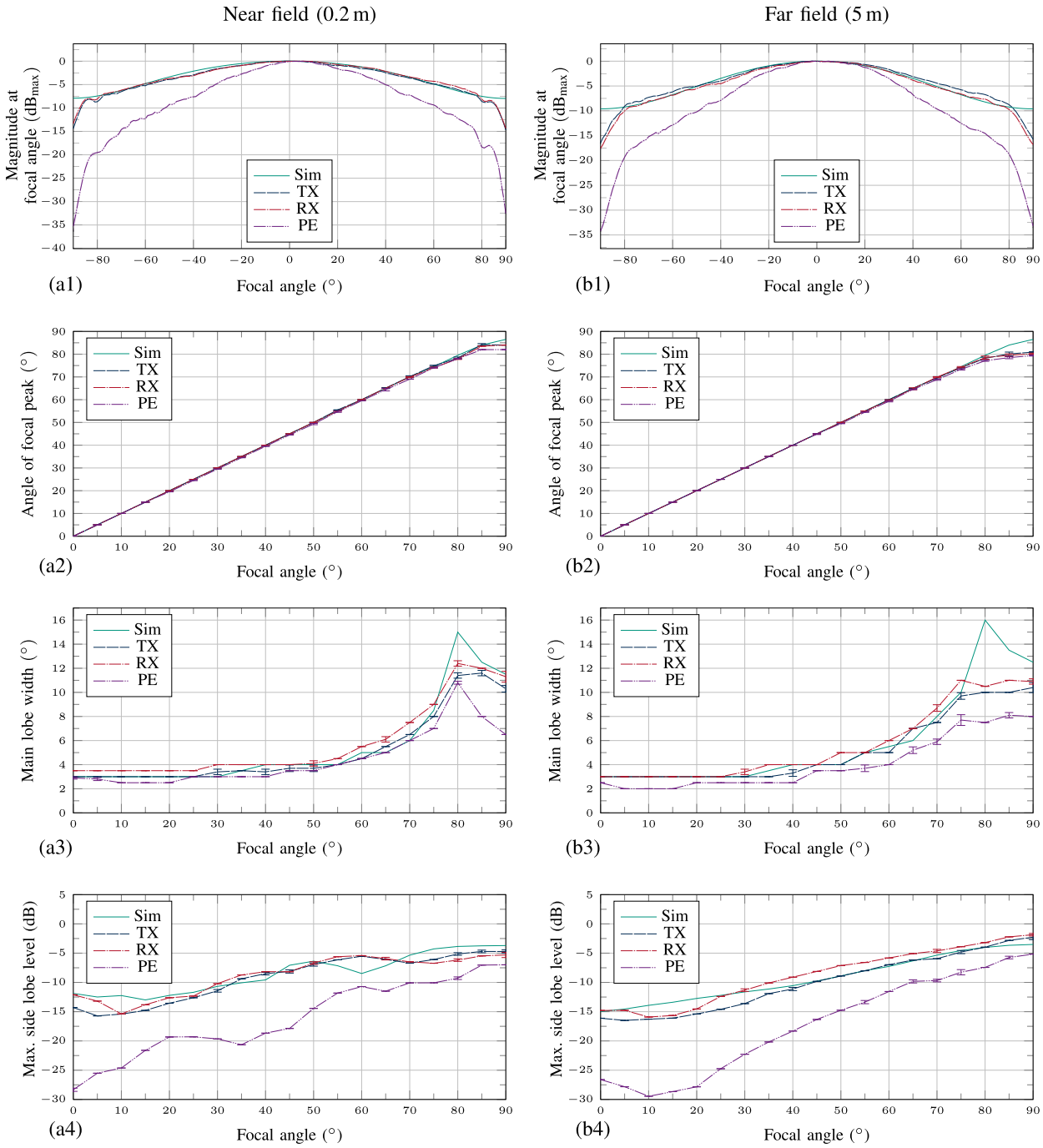

FIGURE 5. **Extracted key parameters from the sectional directivity patterns as shown in (Fig. 4) for all operation modes and the simulation. All values shown are averaged over five measurements. The error bars and shading indicate the corresponding standard deviation. The microphone is used for characterizing the TX mode, the ultrasonic transducer for the RX mode, the small sphere (ϕ50 mm) for the near-field PE mode, and the corner reflector for the far-field PE mode [Fig. 2(a),(b),(c),(e)]. The directivity of the single transducers affects all parameters with increasing focal angles, i.e. the magnitude at the focal angle is reduced (a1),(b1), the angle of the focal peak deviates for focal angles $|\theta| > 80°$ (a2),(b2), the MLW reaches a plateau for focal angles $|\theta| > 80°$ (a3),(b3), and the MSLL rises (a4),(b4). Major differences between measurements and expected values mainly occur for high focal angles $> 80°$ due to the transducer housing which is not included in the simulation. The housing causes an additional attenuation in the peripheral transducer directivity, evident in (a1),(b1) between 80° to 90°. Likewise, this causes simulation mismatches in the other parameter measurements in the same angular range. The measurements and simulations of the MSLL are in good agreement. In general, the values of the PE measurements are approximately two times lower in dB scale due to the two-fold spatial filtering. Overall, the highest beamforming accuracy is achieved for focal angles up to 75° (a2),(b2) and the highest precision for focal angles up to 55° (a3),(b3).**

The radial magnitude distributions measured are shown for the TX mode and selected focal distances in [Fig. 6(a)] as an example. With increasing focal distance, the following effects are observed. First, the maximum magnitude at the respective focal distance decreases due to the attenuation of the medium. As a result, the MSLL out of the focal point steadily increases. The −3 dB focal length widens, reducing the distance selectivity of the focal point. Furthermore, the distance of the focal peak to the desired focal distance starts to diverge for focal distances higher than 0.5 m.

Next, the key parameters extracted from the radial on-axis patterns are analyzed, i.e. the magnitude at the focal distance, the distance of focal peak, focal length and MSLL. First, the magnitude at the focal distance is examined [Fig. 6(b)]. For easy comparison, the respective measurements were normalized to their corresponding value at a distance of 1 m. In addition, the dB values of the PE measurement are adjusted by a factor of 0.5 to account for the doubled propagation path. Due to the measurement setup and the extension of the sphere, the closest focal distance of the PE measurement is 20 cm. The magnitudes at the focal distance of all measurement modes and the simulation are in good agreement. For each mode, a global magnitude maximum exists at different distances, i.e. 10 cm (TX, RX), 28 cm (PE) and 5 cm (Sim). The position of the corresponding maximum is affected by the shape of the respective target. For example, the dimension of the sphere reflector influences the PE measurement for close distances, whereas the simulation assumes an infinitely small target.

The decrease in magnitude for focal points closer to the array than the main maximum is primarily due to the directivity of the individual transducers. With increasing focal distance, the magnitude at the focal distance decreases as well caused by the attenuation of the medium. The PE measurement is attenuated the most due to the doubled propagation path. The differences of the measurements to the simulation arise from atmospheric absorption effects, influenced by temperature, air pressure and humidity [30], which are not represented in the model. Despite the attenuation by the medium, high sound pressure levels are measured by the calibrated microphone in TX mode, i.e. max. 152 dB_{SPL} at 10 cm to min. 119 dB_{SPL} at 5 m distance.

The distance of the focal peak in relation to the desired focal distance indicates the accuracy of the focused beamforming [Fig. 6(c)]. The overall characteristics of all modes are very similar to the simulation. The distance of the focal peak matches the desired focal distance only up to 0.5 m and diverges increasingly for larger distances. Therefore, in order to position the focal peak at a specific distance, a larger focal distance must be selected. However, the focal peak cannot be positioned further than approximately 1 m, as expected for the ϕ200-mm aperture.

The focal length is the range between the −3 dB limits surrounding the focal peak and determines the precision of the focused beamforming, which degrades with increasing focal distance [Fig. 6(d)]. The values measured are in good

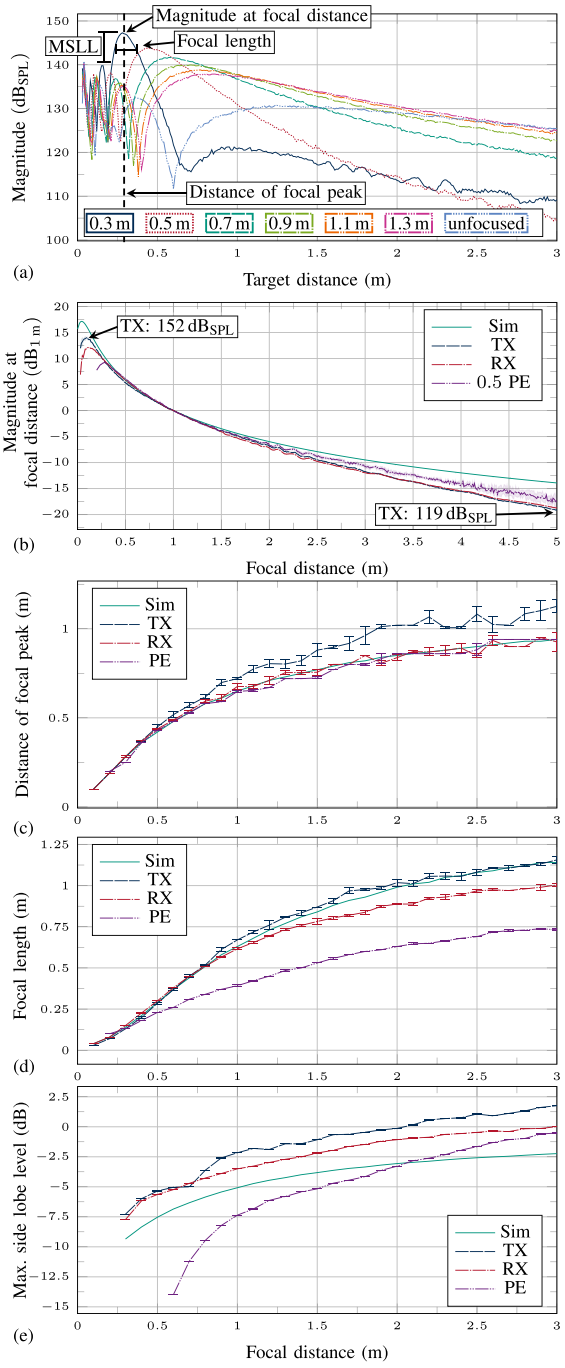

FIGURE 6. Radial on-axis patterns (non-averaged) of the TX mode as an example (a) for varying focal distances in direction (0°, 0°). The parameters marked are extracted and compared for all operation modes in (b)-(e). The values in (b)-(e) are averaged over five measurements. The error bars and shading indicate the corresponding standard deviation. The microphone is used for characterizing the TX mode, the ultrasonic transducer for the RX mode, the sphere (ϕ100 mm) for the PE mode [Fig. 2(a),(b),(d)]. Since the close-range magnitudes measured (b) are affected by the shape of the respective targets, they are normalized to the value at a distance of 1 m for easy comparison. Additionally, the dB values of the PE measurement are adjusted by a factor of 0.5 to account for the doubled propagation path.

agreement with the simulation. The focal length of the PE measurement is significantly lower than the other measurements for all focal distances primarily due to the two-fold spatial filtering. Depending on the specific application, the focal length characteristics measured can be used to determine whether focusing at a certain distance is feasible or generally required.

Finally, the MSLL is analyzed, i.e. the ratio between the magnitude of the focal peak and the corresponding highest local maximum outside the focal zone [Fig. 6(e)]. Therefore, a high MSLL implies a degraded selectivity of the focused beamforming as well. Compared to the simulation, the qualitative characteristics of all measurements are similar. The MSLL of the TX and RX measurements are approximately 3 dB higher than the simulation values, whereas the PE MSLL is generally lower due to the two-fold spatial filtering. The general differences between simulation and measurement are additionally caused by amplitude and phase deviations between the single transducers. For all extracted parameters, the standard deviations obtained from five measurements do not show significant irregularities.

Next, the parameters examined are interpreted for an imaging application using the PE mode. First, it is possible to detect the test sphere (ϕ100 mm) [Fig. 2(d)] in the entire measurement range between 20 cm to 5 m with an appropriate focal distance [Fig. 6(b)]. For imaging, it is often preferred to scan the complete ROI using as few transmission events as possible in order to reduce the measurement time. Therefore, a long and uniform focal zone is advantageous, since objects in a larger range can be detected by a single pulse. Using unfocused beamforming, the longest focal length is achieved and thus the largest range is covered. However, objects with a distance of less than 1 m can not be detected with this method, as its radial on-axis pattern shows several notches in this range [Fig. 6(a)]. Therefore, a reliable detection in the near-field can only be ensured using additional focused pulses with appropriately close focal distances. Due to the decreasing focal length with decreasing focal distance, multiple sequential pulse transmissions with different focal distances are required. For example, in order to cover a viewing range from 20 cm to 5 m, pulses must be focused at least to the distances 0.3 m and 0.5 m in addition to unfocused beamforming. In summary, although the large aperture of the spiral array is advantageous for the achievable angular resolution, additional transmission events are required for detection in the extended near-field.

E. ANGULAR RESOLUTION

The achievable angular resolution using the PE method is experimentally validated. The angular resolution specifies the minimum angular distance between two objects required so that they appear separated in the image generated. For separation, the echoes in the image must create two distinct local maxima. In this experiment, we analyze the relative level of the local minimum between the echo maxima as a function of angular distance between two objects. Two small spheres (ϕ50 mm) [Fig. 2(e)] are used as targets. Their reflection points are positioned at a distance of 2 m in front of the array center. The spheres are mounted on a transverse profile to allow the spacing between the sphere reflection points to be increased symmetrically relative to the z-axis in steps of 2 cm from 6 to 20 cm. For each sphere spacing, a 2D scan is performed from $-10°$ to $+10°$ with an angular step size of 0.2° and a focal distance of 2 m. Each measurement is repeated 20 times to determine the mean level and standard deviation of the local minimum.

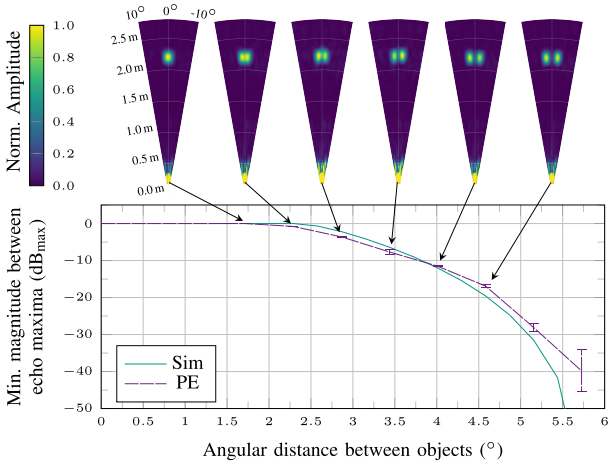

FIGURE 7. Results of the angular resolution measurement using the two spheres [Fig. 2(f)] whose angular spacing is gradually increased at a distance of 2 m. In the B-scans (top), the echoes of the spheres are imaged as two distinct local maxima starting from an angular distance of 2.3°. The lower the minimum magnitude between the echo maxima (bottom), the more reliably they are distinguished by separation algorithms. The values shown are averaged over 20 measurements. The error bars indicate the corresponding standard deviation, which rises with decreasing magnitude starting from −30 dB due to the noise floor.

With a spacing of 6 cm, corresponding to an angular distance of 1.7°, the spheres are not yet separable, as they appear as joint echo without a local minimum (Fig. 7). Starting from a spacing of 10 cm (2.3°) a local minimum with a relative level of $-0.78\,\mathrm{dB_{max}}$ (90%) is formed. Therefore, the determined angular resolution is in good agreement with the −3 dB main lobe width measured [Fig. 5(b3)]. However in practice, often a higher margin between local minimum and maxima is required for a reliable separation, depending on the separation algorithm and additional image processing used. Overall, the results are in good agreement with the expected values from the simulation and the previous MLW measurements.

F. MULTI-REFLECTOR SCENES IN THE FAR- AND NEAR-FIELD

In order to provide a more vivid interpretation of the measurement data obtained and the resulting imaging capabilities,

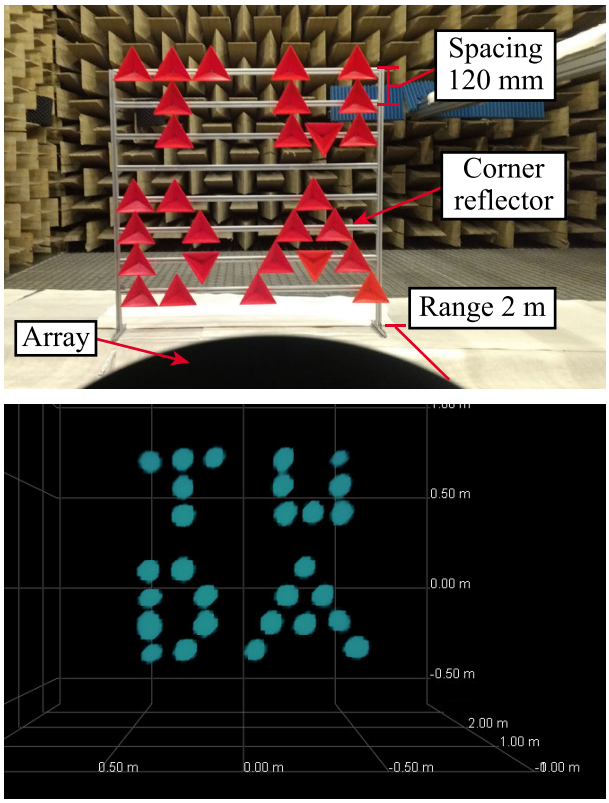

FIGURE 8. Multi-reflector setup consisting of 28 corner reflectors for analyzing the separability and the accumulation of side lobes in the far-field (top). The angular resolution, the accumulated MSLL and the echo intensities of all reflectors are sufficient to correctly separate and visualize the reflector echoes without side lobe artifacts in the OpenGL-rendered 3D-Scan by using a threshold for separation (bottom).

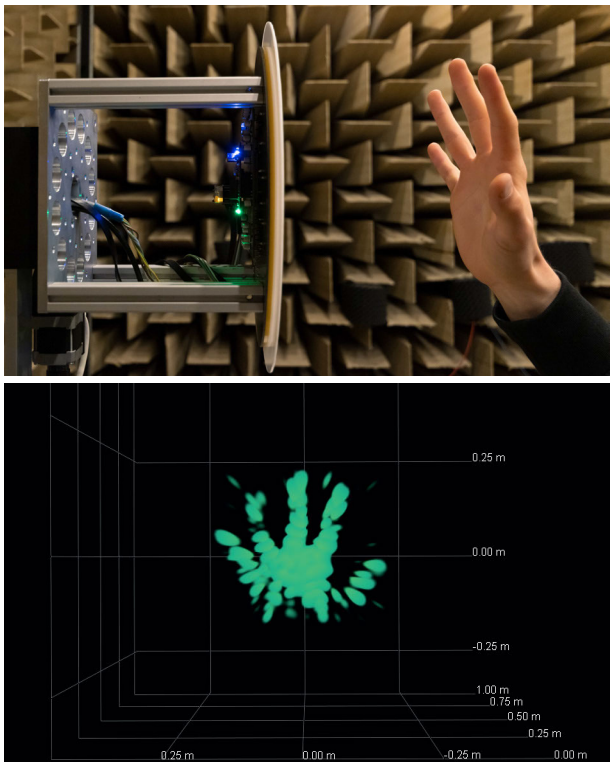

FIGURE 9. Experimental setup for examining the imaging of object shapes in the near-field at 20 cm using focused beamforming. The angular resolution is sufficient to recognize the shape of the hand in the 3D scan. However, the magnitudes of several accumulated side lobes are to some extent higher than the desired echo levels, causing minor artifacts between the fingers. Therefore, if a threshold is used for separation, a trade-off must be found between the level of detail and tolerable artifacts.

we conduct two experiments with multiple reflectors in the far- and near-field. In addition to analyzing the separability, we also investigate the creation of artifacts due to the accumulation of side lobes.

In the far-field experiment, we use a test pattern consisting of 28 corner reflectors positioned at a distance of 2 m in front of the array (Fig. 8). The entire pattern covers a width of 850 mm and is thus located within an angular range of $\pm 12°$ of the ROI. The corner reflectors are identical trihedrals with a front edge length of 140 mm, arranged with a minimum spacing of 120 mm. The spacing corresponds to a minimum angular distance of (3.4°) and is thus slightly above the measured required angular resolution of approximately (2.3°). The scene is scanned line by line using unfocused beamforming in PE mode with an angular step size of 0.5° and visualized in a 3D scan. The total duration for the image generation including data acquisition, processing and rendering is 2 min.

In the image generated, the relative echo magnitudes of the individual reflectors vary between -4 and $0\,\mathrm{dB_{max}}$. The highest minimum between two reflectors is $-5\,\mathrm{dB_{max}}$. Due to the accumulation of the side lobes of the individual reflectors, the MSLL is $-7.3\,\mathrm{dB_{max}}$. Therefore, by using a simple separation threshold between -4 and $-5\,\mathrm{dB_{max}}$, all reflector echoes in this example scene can be separated correctly and no false detections due to side lobe artifacts occur. The experiment illustrates that the accumulated MSLL can increase significantly compared to a single reflector scenario (approx. $-28\,\mathrm{dB_{max}}$), making a clear separation more difficult. Therefore, in the presence of multiple reflectors, the dynamic range is limited, which can lead to either false detections or weaker reflections not being detectable, depending on the separation algorithm and additional image processing used.

The improved angular resolution due to the larger array aperture enables especially close objects to be visualized with high detail. This is demonstrated in another experiment,

TABLE 1. Main characteristics of the spiral and waveguide array.

	Spiral array	Waveguide array		Remark
Aperture	⌀200 mm	35 mm×35 mm	[36]	
TX SPL	148 dB	145 dB	[32]	at 0.3 m
TX MLW	3°	21°	[36]	far-field
RX MLW	3°	12°	[36]	”
TX MSLL	−16.1 dB	−7.2 dB	[36]	”
RX MSLL	−14.8 dB	−11.5 dB	[36]	”
Angular res.	2.3°	12°	[36]	”
Field of view	±80°	±90°	[36]	”

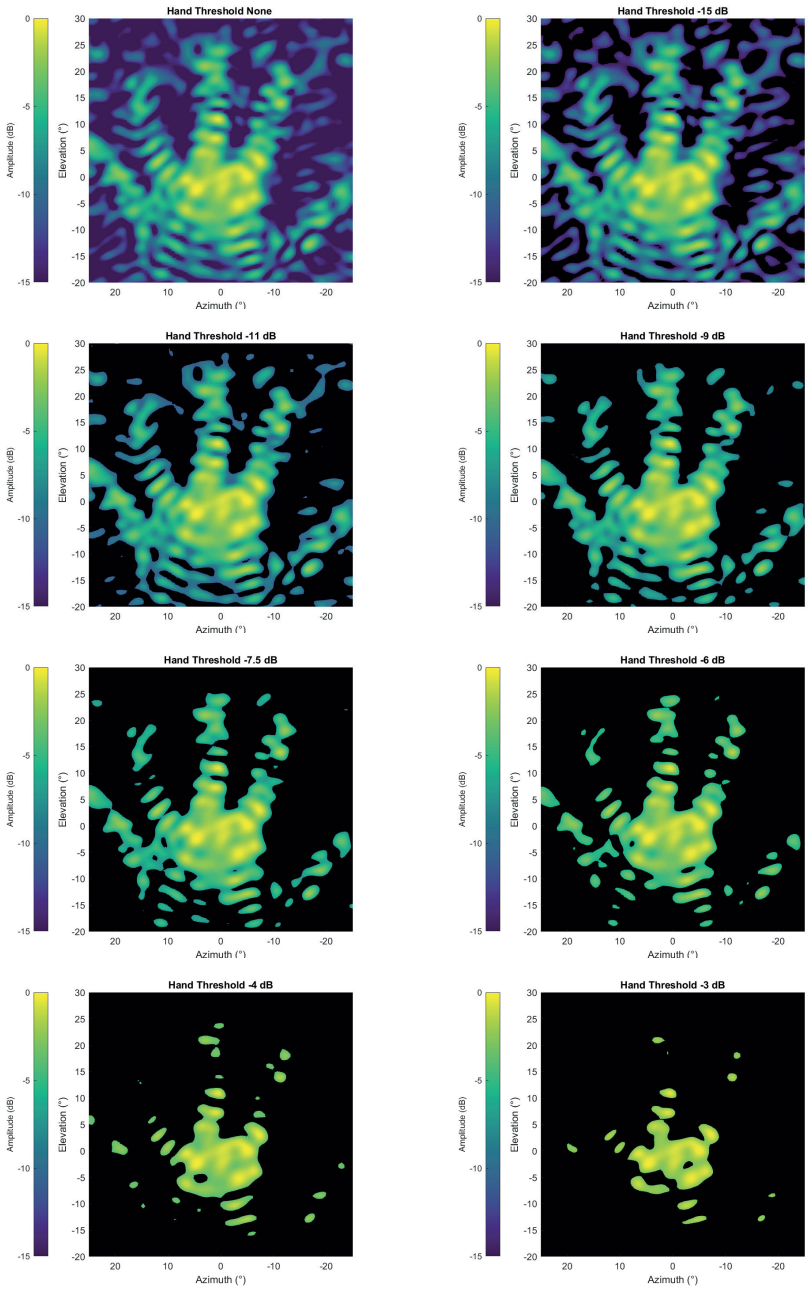

FIGURE 10. 2D sectional image of the hand for different threshold levels. The top left graphic shows the unprocessed raw image of the hand using a dB scale normalized to the highest amplitude received. Only a threshold is used for separating the hand reflections from side lobe artifacts. Amplitudes below the threshold are removed from the image (black color). The higher the threshold is set, the more side lobe artifacts are removed. However, since there are strong and weak hand reflections, some parts of the hand will be removed as well if the threshold is set too high. Therefore, in scenes with a high dynamic range, a trade-off between the level of detail and the accepted artifacts must be found.

where a hand is scanned using focused beamforming at a distance of 20 cm with an angular step size of 0.5° and displayed as a 3D scan (Fig. 9). Compared to the previous measurement setup, the number of retroreflective surfaces can not be exactly defined. The stretched hand has a maximum extension of 19 cm in both dimensions and is thus located in an angular range of ±25°. The length of the fingers is 6 to 8.5 cm with a spacing between them of min. 1 cm to max. 5 cm, corresponding to 2.9° to 14° angular distance. The total time required for generating the image is 2.5 min.

Although the shape of the hand is recognizable in the 3D scan, especially the ring finger and the lower palm are weak

reflectors, since their surface normals partially point away from the array, thus deflecting a large portion of the sound. As a result, the magnitudes of several accumulated side lobes are to some extent higher (MSLL $-5.7\,\mathrm{dB_{max}}$) than the desired reflections (e.g. $-7.2\,\mathrm{dB_{max}}$ at the ring finger center). Therefore, in scenes with a high dynamic range, a trade-off between the level of detail and the accepted artifacts must be found. In the 3D scan shown, a simple separation approach with an example threshold level of $-7.5\,\mathrm{dB_{max}}$ is used, so that few artifacts are visible, but the hand is displayed in more detail. The image processed with different threshold levels is included in the appendix. Overall, the two multi-reflector experiments demonstrated that the array is capable of imaging object shapes and patterns in both the near-field and far-field.

Finally, we put the main characteristics of the sparse spiral array in relation to our previous dense uniform rectangular waveguide array which also consists of 64 MA40S4S transducers and the identical electronic hardware (Table 1). All values, except the field of view, are given for a steering angle of $(0°, 0°)$. At the cost of a larger overall aperture, the MLW, angular resolution and MSLL of the spiral array are significantly improved compared to the uniform rectangular approach. On the other hand, the waveguide array offers additional protection of the transducers and a larger field of view due to the smaller effective element apertures.

IV. CONCLUSION AND FUTURE WORK

We presented an air-coupled spiral ultrasonic phased array system capable of transmit, receive, and pulse-echo operation, as well as 3D imaging. We showed that the large-aperture spiral geometry provides grating lobe free, high-accuracy and high-precision beamforming in all operation modes and is thus valuable for many ultrasonic applications. Especially in-air imaging benefits from these features as they allow unambiguous, high-resolution images to be generated without requiring an increased system complexity or computational load. The SLT technique and the resulting array gains enable a high range of view, so that a large volume can be imaged, spanning the near- and far-field. We demonstrated that even object shapes and patterns of multiple reflectors are recognizable in the images generated, opening up further possibilities, e.g. ultrasonic object classification in harsh environments using deep learning techniques. We found that a more uniform transducer directivity can improve the beamforming and imaging performance, as it increases the field of view, the accuracy and dynamic range for high steering angles. Future work is aimed at improving the frame rate and reducing the MSLL to prevent side lobe artifacts in scenes with multiple reflectors of varying strengths.

APPENDIX

See Fig. 10.

REFERENCES

[1] D. Sancho-Knapik, "Air-coupled ultrasonic resonant spectroscopy for the study of the relationship between plant leaves' elasticity and their water content," *IEEE Trans. Ultrason., Ferroelectr., Freq. Control*, vol. 59, no. 2, pp. 319–325, Feb. 2012.

[2] B. C. Barry, L. Verstraten, F. T. Butler, P. M. Whelan, and W. M. D. Wright, "The use of airborne ultrasound for varroa destructor mite control in beehives," in *Proc. IEEE Int. Ultrason. Symp. (IUS)*, Oct. 2018, pp. 1–9.

[3] A. M. Ginel and T. G. Alvarez-Arenas, "Air-coupled transducers for quality control in the food industry," in *Proc. IEEE Int. Ultrason. Symp. (IUS)*, Oct. 2019, pp. 803–806.

[4] L. Fariñas, M. Contreras, V. Sanchez-Jimenez, J. Benedito, and J. V. Garcia-Perez, "Use of air-coupled ultrasound for the non-invasive characterization of the textural properties of pork burger patties," *J. Food Eng.*, vol. 297, May 2021, Art. no. 110481.

[5] S. Surappa, M. Tao, and F. L. Degertekin, "Analysis and design of capacitive parametric ultrasonic transducers for efficient ultrasonic power transfer based on a 1-D lumped model," *IEEE Trans. Ultrason., Ferroelectr., Freq. Control*, vol. 65, no. 11, pp. 2103–2112, Nov. 2018.

[6] A. S. Rekhi, B. T. Khuri-Yakub, and A. Arbabian, "Wireless power transfer to millimeter-sized nodes using airborne ultrasound," *IEEE Trans. Ultrason., Ferroelectr., Freq. Control*, vol. 64, no. 10, pp. 1526–1541, Oct. 2017.

[7] D. Yosra *et al.*, "Contactless acoustic power transmission through air/skin interface: A feasibility study," in *Proc. IEEE Int. Ultrason. Symp.*, Sep. 2020, pp. 1–3.

[8] A. Ens and L. M. Reindl, "Multicarrier airborne ultrasound transmission with piezoelectric transducers," *IEEE Trans. Ultrason., Ferroelectr., Freq. Control*, vol. 62, no. 5, pp. 905–914, May 2015.

[9] W. Jiang and W. M. D. Wright, "Indoor airborne ultrasonic wireless communication using OFDM methods," *IEEE Trans. Ultrason., Ferroelectr., Freq. Control*, vol. 64, no. 9, pp. 1345–1353, Sep. 2017.

[10] S. Kumar and H. Furuhashi, "Long-range measurement system using ultrasonic range sensor with high-power transmitter array in air," *Ultrasonics*, vol. 74, pp. 186–195, Feb. 2017.

[11] Y. Yoshikawa, Y. Yasuda, I. Toru, S. Izumi, and H. Kawaguchi, "12.5-m distance measurement in high-interference environment using ultrasonic array sensors," in *Proc. IEEE Int. Instrum. Meas. Technol. Conf.*, May 2021, pp. 1–6.

[12] G.-L. Luo, Y. Kusano, and D. A. Horsley, "Airborne piezoelectric micromachined ultrasonic transducers for long-range detection," *J. Microelectromech. Syst.*, vol. 30, no. 1, pp. 81–89, Feb. 2021.

[13] B. W. Drinkwater and P. D. Wilcox, "Ultrasonic arrays for non-destructive evaluation: A review," *NDT E Int.*, vol. 39, pp. 525–541, Oct. 2006.

[14] S. N. Ramadas, J. C. Jackson, J. Dziewierz, R. O'Leary, and A. Gachagan, "Application of conformal map theory for design of 2-D ultrasonic array structure for ndt imaging application: A feasibility study," *IEEE Trans. Ultrason., Ferroelectr., Freq. Control*, vol. 61, no. 3, pp. 496–504, Mar. 2014.

[15] T. Marhenke *et al.*, "Air-coupled ultrasound time reversal (ACU-TR) for subwavelength nondestructive imaging," *IEEE Trans. Ultrason., Ferroelectr., Freq. Control*, vol. 67, no. 3, pp. 651–663, Mar. 2020.

[16] K. Hasegawa and H. Shinoda, "Aerial vibrotactile display based on multiunit ultrasound phased array," *IEEE Trans. Haptics*, vol. 11, no. 6, pp. 367–377, Jul. 2018.

[17] R. Hirayama, D. Martinez Plasencia, N. Masuda, and S. Subramanian, "A volumetric display for visual, tactile and audio presentation using acoustic trapping," *Nature*, vol. 575, pp. 320–323, Nov. 2019.

[18] R. Morales, I. Ezcurdia, J. Irisarri, M. A. B. Andrade, and A. Marzo, "Generating airborne ultrasonic amplitude patterns using an open hardware phased array," *Appl. Sci.*, vol. 11, p. 2981, Mar. 2021.

[19] A. Marzo, S. A. Seah, B. W. Drinkwater, D. R. Sahoo, B. Long, and S. Subramanian, "Holographic acoustic elements for manipulation of levitated objects," *Nature Commun.*, vol. 6, Dec. 2015, Art. no. 8661.

[20] A. Watanabe, K. Hasegawa, and Y. Abe, "Contactless fluid manipulation in air: Droplet coalescence and active mixing by acoustic levitation," *Sci. Rep.*, vol. 8, Dec. 2018, Art. no. 10221.

[21] T. Kasai, T. Furumoto, and H. Shinoda, "Rotation and position control of a cubic object using airborne ultrasound," in *Proc. IEEE Int. Ultrason. Symp.*, Sep. 2020, pp. 1–4.

[22] I. Wygant *et al.*, "50 kHz capacitive micromachined ultrasonic transducers for generation of highly directional sound with parametric arrays," *IEEE Trans. Ultrason. Ferroelectr., Freq. Control*, vol. 56, no. 1, pp. 193–203, Jan. 2009.

[23] K. Nakagawa, C. Shi, and Y. Kajikawa, "Beam steering of portable parametric array loudspeaker," in *Proc. Asia–Pacific Signal Inf. Process. Assoc. Annu. Summit Conf.*, Nov. 2019, pp. 1824–1827.

[24] Z. Shao, S. Pala, Y. Liang, Y. Peng, and L. Lin, "A single chip directional loudspeaker based on PMUTS," in *Proc. IEEE Int. Conf. Micro Electro Mechan. Syst.*, Jan. 2021, pp. 895–898.

[25] V. Kunin, M. Turqueti, J. Saniie, and E. Oruklu, "Direction of arrival estimation and localization using acoustic sensor arrays," *J. Sens. Technol.*, vol. 1, Oct. 2011, Art. no. 7657.

[26] G. Allevato, M. Rutsch, J. Hinrichs, M. Pesavento, and M. Kupnik, "Embedded air-coupled ultrasonic 3d sonar system with GPU acceleration," in *Proc. IEEE Sens.*, Oct. 2020, pp. 1–4.

[27] T. Verellen, R. Kerstens, and J. Steckel, "High-resolution ultrasound sensing for robotics using dense microphone arrays," *IEEE Access*, vol. 8, pp. 190083–190093, 2020.

[28] H. Zhang, D. Liang, Z. Wang, L. Ye, X. Rui, and X. Zhang, "Fabrication and characterization of a wideband low-frequency CMUT array for air-coupled imaging," *IEEE Sensors J.*, vol. 20, no. 23, pp. 14090–14100, Dec. 2020.

[29] O. J. Adelegan, Z. A. Coutant, X. Wu, F. Y. Yamaner, and O. Oralkan, "Design and fabrication of wideband air-coupled capacitive micromachined ultrasonic transducers with varying width annular-ring and spiral cell structures," *IEEE Trans. Ultrason., Ferroelectr., Freq. Control*, vol. 68, no. 8, pp. 2749–2759, Aug. 2021.

[30] H. E. Bass, L. C. Sutherland, and A. J. Zuckerwar, "Atmospheric absorption of sound: Update," *J. Acoust. Soc. Amer.*, vol. 88, no. 4, pp. 2019–2021, Oct. 1990.

[31] M. Rutsch *et al.*, "Waveguide for air-coupled ultrasonic phased-arrays with propagation time compensation and plug-in assembly," *J. Acoust. Soc. Amer.*, vol. 150, no. 5, pp. 3228–3237, Nov. 2021.

[32] A. Jäger *et al.*, "Air-coupled 40 kHz ultrasonic 2D-phased array based on a 3D-printed waveguide structure," in *Proc. IEEE Int. Ultrason. Symp.*, Sep. 2017, pp. 1–4.

[33] G. Allevato *et al.*, "3D imaging method for an air-coupled 40 kHz ultrasound phased-array," in *Proc. Int. Congr. Acoust.*, 2019, pp. 1–8.

[34] C. Haugwitz *et al.*, "Flow metering of gases using ultrasonic phased-arrays at high velocities," in *Proc. IEEE Int. Ultrason. Symp.*, Oct. 2019, pp. 1129–1132.

[35] A. Jäger *et al.*, "Non-contact ultrasound with optimum electronic steering angle to excite Lamb waves in thin metal sheets for mechanical stress measurements," in *Proc. Int. Ultrason. Symp.*, Oct. 2019, pp. 924–927.

[36] G. Allevato *et al.*, "Real-time 3-D imaging using an air-coupled ultrasonic phased-array," *IEEE Trans. Ultrason. Ferroelectr., Freq. Control*, vol. 68, no. 3, pp. 796–806, Mar. 2021.

[37] M. Rutsch, G. Allevato, J. Hinrichs, and M. Kupnik, "Protection layer for air-coupled waveguide ultrasonic phased arrays," in *Proc. IEEE Int. Ultrason. Symp.*, Sep. 2020, pp. 1–4.

[38] P. Weber, R. Schmitt, B. Tylkowski, and J. Steck, "Optimization of random sparse 2-D transducer arrays for 3-D electronic beam steering and focusing," in *Proc. IEEE Ultrason. Symp.*, Oct. 1994, pp. 1503–1506.

[39] R. Davidsen, "Two-dimensional random arrays for real time volumetric imaging," *Ultrason. Imag.*, vol. 16, pp. 143–163, Jul. 1994.

[40] A. Austeng and S. Holm, "Sparse 2-D arrays for 3-D phased array imaging-design methods," *IEEE Trans. Ultrason. Ferroelectr., Freq. Control*, vol. 49, no. 8, pp. 1073–1086, Aug. 2002.

[41] D. W. Boeringer, "Phased array including a logarithmic spiral lattice of uniformly spaced radiating and receiving elements," U.S. Patent 6 433 754 B1, Aug. 13, 2002.

[42] M. C. Viganó, G. Toso, G. Caille, C. Mangenot, and I. E. Lager, "Sunflower array antenna with adjustable density taper," *Int. J. Antennas Propag.*, vol. 2009, Apr. 2009, Art. no. 624035.

[43] E. Sarradj, "A generic approach to synthesize optimal array microphone arrangements," in *Proc. Berlin Beamforming Conf.*, 2016, pp. 1–4.

[44] A. Vallecchi, M. Cerretelli, M. Linari, and G. B. Gentili, "Investigation of optimal array configurations for full azimuth scan HF skywave radars," in *Proc. 6th Eur. Radar Conf.*, Oct. 2009, pp. 200–203.

[45] Q. Cheng, Y. Liu, H. Zhang, and Y. Hao, "A generic spiral MIMO array design method for short-range UWB imaging," *IEEE IEEE Antennas Wireless Propag. Lett.*, vol. 19, no. 5, pp. 851–855, May 2020.

[46] L. H. Gabrielli and H. E. Hernandez-Figueroa, "Aperiodic antenna array for secondary lobe suppression," *IEEE Photon. Technol. Lett.*, vol. 28, no. 2, pp. 209–212, Jan. 15, 2016.

[47] Z. Lei, "Sound sources localization using compressive beamforming with a spiral array," in *Proc. Int. Conf. Inf. Commun. Technol.*, Apr. 2015, pp. 1–5.

[48] S. Luesutthiviboon, A. Malgoezar, M. Snellen, P. Sijtsma, and D. Simons, "Improving source discrimination performance by using an optimized acoustic array and adaptive high-resolution CLEAN-SC beamforming," in *Proc. Berlin Beamforming Conf.*, 2018, pp. 1–27.

[49] O. Martínez-Graullera, C. J. Martín, G. Godoy, and L. G. Ullate, "2D array design based on Fermat spiral for ultrasound imaging," *Ultrasonics*, vol. 50, pp. 280–289, Feb. 2010.

[50] A. Ramalli, E. Boni, A. S. Savoia, and P. Tortoli, "Density-tapered spiral arrays for ultrasound 3-D imaging," *IEEE Trans. Ultrason. Ferroelectr., Freq. Control*, vol. 62, no. 8, pp. 1580–1588, Aug. 2015.

[51] H. Yoon and T.-K. Song, "Sparse rectangular and spiral array designs for 3D medical ultrasound imaging," *Sensors*, vol. 20, p. 173, Dec. 2019.

[52] A. Ramalli *et al.*, "Real-time 3-D spectral Doppler analysis with a sparse spiral array," *IEEE Trans. Ultrason. Ferroelectr., Freq. Control*, vol. 68, no. 5, pp. 1742–1751, May 2021.

[53] A. Price and B. Long, "Fibonacci spiral arranged ultrasound phased array for mid-air haptics," in *Proc. IEEE Int. Ultrason. Symp.*, Oct. 2018, pp. 1–4.

[54] A. Movahed, T. Waschkies, and U. Rabe, "Air ultrasonic signal localization with a beamforming microphone array," *Adv. Acoust. Vib.*, vol. 2019, Feb. 2019, Art. no. 7691645.

[55] M. Legg and S. Bradley, "Ultrasonic arrays for remote sensing of pasture biomass," *Remote Sens.*, vol. 12, p. 111, Dec. 2019.

[56] B. Parr, M. Legg, S. Bradley, and F. Alam, "Occluded grape cluster detection and vine canopy visualisation using an ultrasonic phased array," *Sensors*, vol. 21, p. 2182, Mar. 2021.

[57] G. Allevato, M. Rutsch, J. Hinrichs, E. Sarradj, M. Pesavento, and M. Kupnik, "Spiral air-coupled ultrasonic phased array for high resolution 3D imaging," in *Proc. IEEE Int. Ultrason. Symp.*, Sep. 2020, pp. 1–4.

[58] T. L. Szabo, *Diagnostic Ultrasound Imaging: Inside Out*, 2nd ed. Amsterdam, The Netherlands: Elsevier, 2014.

[59] A. M. Zoubir, M. Viberg, R. Chellappa, and S. Theodoridis, *Array and Statistical Signal Processing*, 1st ed. Amsterdam, The Netherlands: Elsevier Academic Press, 2014.

[60] J. A. Jensen, S. I. Nikolov, K. L. Gammelmark, and M. H. Pedersen, "Synthetic aperture ultrasound imaging," *Ultrasonics*, vol. 44, p. e15, Dec. 2006.

[61] H. Hasegawa and H. Kanai, "High-frame-rate echocardiography using diverging transmit beams and parallel receive beamforming," *J. Med. Ultrason.*, vol. 38, no. 3, pp. 129–140, Jul. 2011.

[62] S. Smith, H. Pavy, and O. Von Ramm, "High-speed ultrasound volumetric imaging system. I. Transducer design and beam steering," *IEEE Trans. Ultrason. Ferroelectr. Freq. Control*, vol. 38, no. 2, pp. 100–108, Mar. 1991.

[63] P.-O. Persson and G. Strang, "A simple mesh generator in MATLAB," *SIAM Rev.*, vol. 46, pp. 329–345, Jan. 2004.

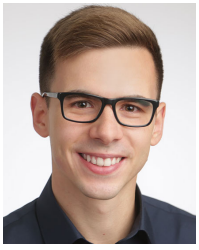

GIANNI ALLEVATO (Student Member, IEEE) received the M.Sc. degree in electrical engineering from Technische Universtität Darmstadt (TU Darmstadt), Germany, in 2018. Since 2018, he has been a Research Associate with the Measurement and Sensor Technology Group, TU Darmstadt. His research interests include electronics and embedded system design, software development, and parallel signal processing for imaging with air-coupled ultrasonic phased arrays and its applications.

MATTHIAS RUTSCH (Graduate Student Member, IEEE) received the B.Sc. degree from Brandenburgische Technische Universität Cottbus–Senftenberg, Germany, in 2014, and the M.Sc. degree in electrical engineering from Technische Universität Darmstadt, in 2017. Since then, he has been a Research Associate at the Measurement and Sensor Technology Group, Technische Universität Darmstadt. His research interests include simulation and characterization of duct acoustics for air-coupled ultrasound applications.

JAN HINRICHS (Graduate Student Member, IEEE) received the M.Sc. degree in electrical engineering from Technische Universität Darmstadt (TU Darmstadt), Germany, in 2017. Since then, he has been a Research Associate with the Measurement and Sensor Technology Group, TU Darmstadt. His research interests include sensor design, sensor electronics, acoustoelastic sensing, and non-destructive examination using Lamb waves.

CHRISTOPH HAUGWITZ (Student Member, IEEE) received the M.Sc. degree in electrical engineering from Technische Universität Darmstadt (TU Darmstadt), Germany, in 2021. Since then, he has been a Research Associate with the Measurement and Sensor Technology Group, TU Darmstadt. His research interests include ultrasonic flow metering and air-coupled ultrasonic phased arrays and its applications.

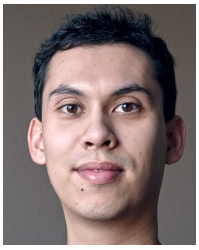

RAPHAEL MÜLLER received the M.Sc. degree in electrical engineering from Technische Universität Darmstadt (TU Darmstadt), Germany, in 2020. Since then, he has been a Research Associate at the Communication Systems Group, TU Darmstadt. His research interests include statistical signal processing and especially high-resolution sensor array processing and its application to radar and ultrasound.

MARIUS PESAVENTO (Senior Member, IEEE) received the Dipl-Ing. degree from Ruhr-Universität Bochum, Bochum, Germany, in 1999, the M.Eng. degree from McMaster University, Hamilton, ON, Canada, in 2000, and the Dr.-Ing. degree in electrical engineering from Ruhr-Universität Bochum, in 2005. From 2005 to 2009, he was a Research Engineer with two startup companies. In 2010, he was an Assistant Professor of robust signal processing and a Full Professor of communication systems, in 2013, with the Department of Electrical Engineering and Information Technology, Technische Universität Darmstadt, Darmstadt, Germany. His research interests include robust signal processing and adaptive beamforming, high-resolution sensor array processing, multi-antenna and multi-user communication systems, distributed, sparse, mixed-integer optimization techniques for signal processing and communications, statistical signal processing, spectral analysis, and parameter estimation.

MARIO KUPNIK (Senior Member, IEEE) received the Dipl.-Ing. degree in electrical engineering from the Graz University of Technology, Graz, Austria, in 2000, and the Ph.D. degree in electrical engineering from the University of Leoben, Leoben, Austria, in 2004. From 2005 to 2011, he was a Postdoctoral Researcher, a Research Associate, and a Senior Research Scientist at the Edward L. Ginzton Laboratory, Stanford University, Stanford, CA, USA. From 2011 to 2014, he was a Full Professor of electrical engineering at the Brandenburg University of Technology, Cottbus, Germany. Since 2015, he has been a Full Professor at Technische Universität Darmstadt, Darmstadt, Germany, where he is currently the Head of the Measurement and Sensor Technology Group. His research interests include micro-machined sensors and actuators, multi-physics simulations, flow-metering of gases and liquids, ultrasound, electroacoustics, and harsh-environment instrumentation.